Temperature-Dependent Frictional Behavior of MoS$_2$ in Humid Environments: Insights from Water Molecule Adsorption and DFT Analyses

Zaixiu Yang, Xingkai Zhang, Kaixiong Gao, Bin Zhang,* Fatih G. Sen, Sukanta Bhowmick, Junyan Zhang,* and Ahmet T. Alpas*

ACCESS | Metrics & More | Article Recommendations | Supporting Information

ABSTRACT: This study investigates the temperature-dependent frictional behavior of MoS$_2$ in humid environments within the context of a long-standing debate over increased friction due to oxidation processes or molecular adsorption. By combining sliding friction experiments and density functional theory (DFT)-based first-principles simulations, it aims to clarify the role of water molecule adsorption in influencing frictional properties of MoS$_2$, addressing the challenge of identifying interfacial bonding behavior responsible for friction in such conditions. Sliding experiments revealed that magnetron-sputtered MoS$_2$ exhibits a reduction in the coefficient of friction (COF) with an increase in temperature from 25 to 100 °C under 20 and 40% relative humidity. This change in the COF obeys the Arrhenius law, presenting an energy barrier of 0.165 eV, indicative of the temperature-dependent nature of these frictional changes and suggests a consistent frictional mechanism. DFT simulations showed that H$_2$O molecules are adsorbed at MoS$_2$ vacancy defects with adsorption energies ranging from −0.56 to −0.17 eV, which align with the experimentally determined energy barrier. Adsorptive interactions, particularly the formation of stable H···S interfacial hydrogen bonds at defect sites, increase the interlayer adhesion and impede layer shearing. TEM analysis confirms that although MoS$_2$ layers align parallel to the sliding direction in humid conditions, the COF remains at 0.12, as opposed to approximately 0.02 in dry air. This demonstrates that parallel layer alignment does not notably decrease the COF, underscoring humidity's significant role in MoS$_2$'s COF values, a result also supported by the Arrhenius analysis. The reversibility of the physisorption process, demonstrated by the recovery of the COF in high-temperature humid environments, suggests its dynamic nature. This study yields fundamental insights into MoS$_2$ interfaces for environments with variable humidity and temperature, crucial for demanding tribological applications.

KEYWORDS: molybdenum disulfide, water molecule, adsorption, friction mechanisms, surface vacancies, interfacial hydrogen bonding
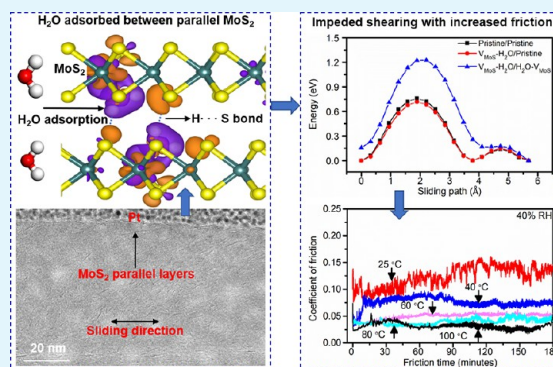
1. INTRODUCTION

Molybdenum disulfide (MoS$_2$) is widely investigated for its various applications including as a catalyst for hydrogen reduction and molecule sensing and as a dry and liquid-based lubricant.[1−3] Due to its low friction in vacuum and inert atmospheres, MoS$_2$ is a preferred solid lubricant for gears and bearings in space applications.[4,5] The low friction of MoS$_2$ in vacuum and dry environments has been commonly attributed to the easy shearing of parallel-oriented MoS$_2$ layers bonded by van der Waals forces.[6−8] However, the lubricity of MoS$_2$ deteriorates significantly with humidity due to increased friction and wear.[9] Early work showed that the interaction of oxygen and water molecules with MoS$_2$ at defects sites (such as edge) initiates oxidation of MoS$_2$, leading to the formation of molybdenum trioxide (MoO$_3$) and gas products.[10,11] With the formation of nonlubricating MoO$_3$ observed after long-term storage or during friction processes in humid environments,

the oxidation process is widely considered as one of the main reasons responsible for the increased friction of MoS$_2$.[12,13]

The amount of MoO$_3$ formed during tribological testing of MoS$_2$ may not be significant, especially when compared to the oxidation observed during prolonged exposure in humid environments, since the friction process requires overcoming high energy barriers for molecular dissociation at low temperatures.[14,15] Oxidation of MoS$_2$ to MoO$_3$ was not observed in an in situ Raman investigation of the MoS$_2$ film after 6500 sliding cycles in a friction test performed at 330
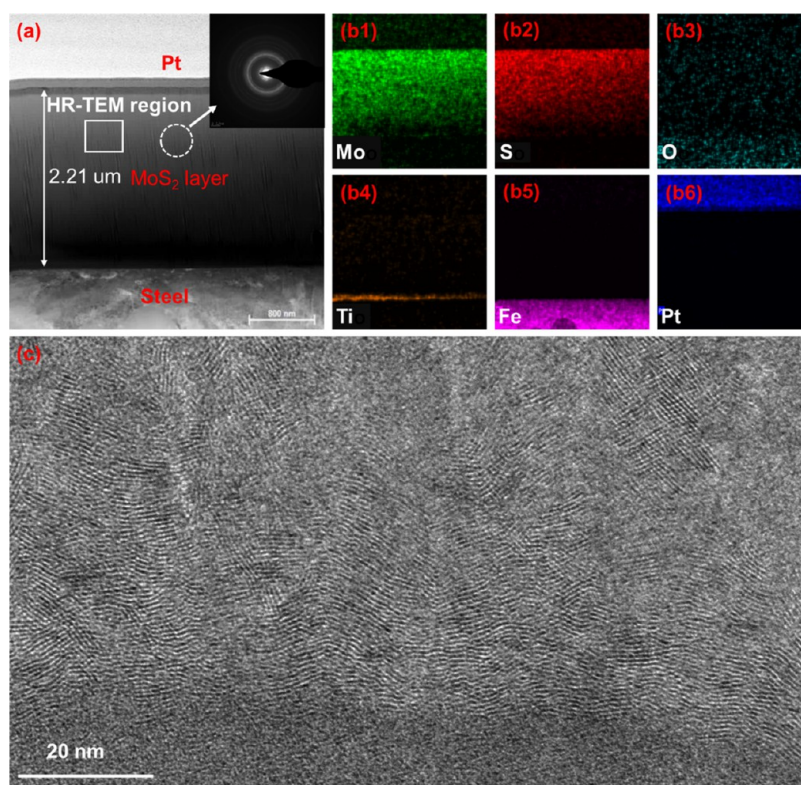
Figure 1. (a) Low-magnification cross-sectional TEM image of the MoS$_2$ coating deposited on 304 stainless steel, with a selected area electron diffraction pattern inset. (b) EDX elemental mapping of (a) showing elements of Mo (b1), S (b2), O (b3), Ti (b4), Fe (b5), and Pt (b6). (c) HR-TEM image taken from the boxed region in plate (a).

°C.[16] This finding challenges the prevailing assumption that oxidation is the primary cause of increased friction in MoS$_2$. Contrasting the oxidation mechanism traditionally thought to increase MoS$_2$'s friction, atomic force microscopy (AFM) studies and first-principles computations have revealed the formation of incommensurate contact between MoS$_2$ and MoO$_3$. This interaction results in structural superlubricity, evidenced by a coefficient of friction (COF) less than 0.01, attributable to lower layer shearing energy compared to MoS$_2$ layers alone.[14,15] Fleischauer et al.[17] suggested that an increase in oxygen substitution in MoS$_{2-x}$O$_x$ would reduce the friction via smoothing of surface topography and a decrease in the interlayer forces. Therefore, the oxidation process may not be the major or sole cause of the increased friction of MoS$_2$ in humid environments, suggesting the need to explore other mechanisms.

Haltner and Oliver[18] noted that the COF of MoS$_2$ rises with water partial pressure, suggesting that water molecule physisorption might increase shearing strength and friction. Emerging evidence supports the idea that water physisorption rather than the oxidation is the process that significantly increased friction. Atomic force microscopy (AFM) tests of MoS$_2$ confirmed increased MoS$_2$ friction with humidity, without any oxidation.[19,20] Investigations of MoS$_2$ at different temperatures also revealed that the increased friction in humid environments is reversible at temperatures below 100 °C, a behavior that is not expected from chemical reactions.[21,22] Consequently, the process of water adsorption may account for the increased friction observed in MoS$_2$ under humid conditions. However, the challenge of experimentally determining the atomistic-scale structure of water molecules adsorbed between MoS$_2$ layers leaves unanswered questions

about how exactly water adsorption influences MoS$_2$ friction, maintaining the debate on whether adsorption or oxidation is the primary mechanism for increased friction in such environments.

Due to the ability to provide atomistic insights, density functional theory (DFT) computations have been utilized to study how the adsorption of water molecules on and between MoS$_2$ layers influences their sliding behavior and consequently the COF. Defects in exfoliated, CVD-grown, or magnetron-sputtered MoS$_2$ could increase the reactivity of MoS$_2$ and promote molecular adsorption.[23−26] Computational studies showed that the tendency for molecules to adsorb dissociatively or nondissociatively at these defect sites depended on the reactivity of the defects.[27,28] Simulations were also performed to illustrate the H$_2$O adsorption on vacancy sites of MoS$_2$.[29,30] Calculations by Yang et al.[29] have suggested that increased friction of MoS$_2$ in humid conditions was linked to undissociated water molecules forming hydrogen bonds at vacancy defects, raising the interlayer binding energy and friction, a mechanism more influential than water molecule dissociation at these defects. Supporting this mechanism, there was a notable rise in the COF from 0.007 in dry conditions to 0.09−0.11 under ~40% relative humidity, with HR-TEM and Raman spectroscopy providing evidence of water-induced hydrogen bonding between MoS$_2$ layers. Interlayer sliding properties with H$_2$O adsorbed between either pristine or S-vacated layers have been previously investigated,[31,32] and the adsorption of water at these layers was suggested to be thermodynamically unfavored, as it leads to an expansion of the layer spacing and demands additional energy.[33]

The current research work aims to enhance our understanding of how molecular interactions impact the frictional

behavior of MoS_2 under humid conditions at different temperatures. It builds on Yang et al.'s[29] previous work by focusing on how water molecules adsorb onto MoS_2 with existing vacancy defects and the subsequent effect on friction by preforming sliding experiments, characterizing the resulting worn surfaces and transferred material, and employing DFT simulations for interface modeling. Interlayer binding energy and the energy barriers associated with interlayer shearing were evaluated to explore how the presence of adsorbed water molecules modifies these parameters. The reversible nature of water molecule adsorption on MoS_2 and its effect on the COF were considered in order to understand the dynamic behavior of this interaction. Additionally, the DFT investigation characterized the H···S hydrogen bonds formed between water molecules and MoS_2, assessing how these bonds affect layer adhesion and resistance to shearing.

2. METHODS

2.1. Experimental Details. MoS_2 films were deposited on 304 stainless-steel disks, each 2 cm in diameter, using a Teer UDP-650 unbalanced magnetron sputtering system according to the methodology measures while testing the coatings against AISI 52100 steel balls, each 6 mm in diameter, using a tribometer with a heating system (MS-9000, Lanzhou Huahui Instrument Technology Co., Ltd.). The tests were performed under a normal load of 0.3 N in reciprocated sliding mode at a frequency of 5 Hz, under ambient conditions at a relative humidity (RH) of 20 and 40%. The effect of moisture adsorption and desorption on the friction of MoS_2 was evaluated by conducting tests at testing temperatures of 25−100 °C, where the temperature of the furnace was controlled with PID regulators with a temperature error of ±2 °C and tests were not started until the surface temperatures measured using a thermal detector (Bosch GIS 500) reached the designated value. For comparison, dry tests were taken by reducing the chamber's relative humidity to less than 3%, achieved by circulating dry air.

Raman spectroscopy was used to analyze the structural changes in the MoS_2 films before and after the friction tests using a Raman spectrometer (Horiba Jobin Yvon) equipped with a 532 nm laser (see Figure S1 for the as-deposited MoS_2 film). The morphology of the ball surfaces and weak tracks on the MoS_2 were characterized using a scanning electron microscope (Apreo S, SEM) at an accelerating voltage of 15 kV. The internal structures of MoS_2 films and the transfer layers formed on the counterface were analyzed using high-resolution transmission electron microscopy (HR-TEM FEI Tecnai-G2-F20), where the HR-TEM specimens were prepared using the focused ion beam (FIB) technique with a lift-out method. As shown in the cross-sectional images of Figure 1a,b, the MoS_2 with a thickness of 2.21 μm was deposited on top of the steel substrate with a Ti interlayer of ∼0.1 μm. The HR-TEM in Figure 1c revealed that the MoS_2 layer had a nanocrystalline structure mixed with amorphous zones, which is consistent with the ring pattern in the selected area diffraction image (SAED) inset of Figure 1a. The identified defect structure agrees with previous TEM observations in the sputtered MoS_2.[24,29] These defect features are highlighted in this study as playing an essential role in affecting the molecular adsorption processes and consequently frictional behavior.

The role of the defects in the adsorption of H_2O to MoS_2 was investigated by introducing structural defects on MoS_2 plates using a ball milling method. MoS_2 powders (Xianfeng Nano) with an average size of 3−5 μm were placed into ZrO_2 jars and milled for 24 h using ZrO_2 balls at a rotational speed of 200 rpm. To facilitate H_2O adsorption at the generated defects, 10 wt % H_2O was added at the initial stage of the milling process. The milling process which is known for generating defects resulted in observable changes in the structure. Raman spectroscopy of MoS_2 after the ball milling process in Figure S1 confirmed these milling-induced defects as evidenced by the shift of the in-plane E_{2g}^1 from 378 to 377 cm^{-1} and the broadening of the E_{2g}^1 and A_{1g} (∼400 cm^{-1}) modes.[34−36] This preparation allows

for the analysis of H_2O adsorption onto ball-milled MoS_2 layers, offering a reference for understanding the H_2O interaction with defective MoS_2 during the sliding process, although the defect types and concentrations between the ball-milled MoS_2 and the sputtered MoS_2 may differ. The desorption analysis was carried out using thermogravimetric analysis (Netzsch, Germany) in an Al_2O_3 crucible with the temperature increasing from (room temperature) 22 to 600 °C at a rate of 10 °C/min in a dry air atmosphere.

2.2. First-Principles Calculation Methodology. The adsorption behaviors of H_2O at vacancy defect sites of MoS_2 were studied by first-principles calculations in the Vienna Ab initio Simulation Package (VASP).[37] The calculations utilized projector-augmented wave (PAW) pseudopotentials and the generalized gradient approximation (GGA) with the PBE functional.[38,39] The VdW-DF2 density functional within VASP[40−42] known for accurately estimating the interlayer binding energy (E_B) in graphene and MoS_2 systems by considering the van der Waals interaction[43,44] was applied to evaluate the adsorption of H_2O molecules on MoS_2 layers following methodologies from previous work.[29]

Given that 2H-MoS_2 (see the trigonal structure in Figure S2(a)) is thermodynamically more stable than 1T-MoS_2 with its octahedral structure,[45,46] it was selected for use in the computational studies. To investigate the adsorption of H_2O on vacancy sites of MoS_2, a (4×4) supercell of MoS_2 with lateral dimensions of 13.12 Å was constructed, incorporating a 15 Å vacuum layer in the direction normal to the basal plane so that the cell was large enough to prevent interactions between H_2O molecules from periodic images. During the total energy and atomic force minimization process, a plane wave basis set with a kinetic cutoff energy of 500 eV and a kpoint grid of $(5 \times 5 \times 1)$ were utilized. Atomic positions were relaxed until the maximum Hellmann−Feynman force acting on any atom was less than 0.01 eV/Å using the conjugate gradient method, and the total energy between two consecutive steps was converged to 10^{-5} eV. Spin polarization was also included to account for the magnetism induced by the dangling bonds at the vacancy defect sites.

Various vacancy types such as V_S, V_{S2}, V_{Mo}, V_{MoS3}, and V_{MoS6} as well as antisite defects have been identified in monolayer MoS_2 deposited using CVD and PVD methods by means of HR-TEM.[24,25] Thus, to systematically investigate the effects of these defects on the H_2O molecule adsorption and interfacial properties, vacancies of the types V_S, V_{S2}, V_{Mo}, V_{MoS}, and V_{MoS3} were considered in a (4×4) cell. These defects were modeled by removing specific atoms, namely, S^1 for V_S, S^1 and S^2 for V_{S2}, Mo for V_{Mo}, Mo and S^1 for V_{MoS}, and Mo, S^1, S^3, and S^4 for V_{MoS3} as indicated in Figure S2(a). The potential adsorption sites for the H_2O molecule at these defect sites of MoS_2 were investigated by positioning the H_2O molecule at the vacancy center, with initial orientations both parallel and normal to the basal plane of monolayer MoS_2. To account for the potential molecule dissociation at vacancy sites, the H_2O was placed at distances of 0 and 2 Å above the MoS_2 layer, with the distance defined relative to the topmost S layer (using averaged S atom positions) and the nearest H_2O atom. The representative initial configurations with H_2O adsorption with the H_2O molecule at the center of V_{MoS3} oriented both normal and parallel to the MoS_2 (002) plane are shown in Figure S2(b,c). The final adsorption sites were identified by determining the lowest-energy configurations after system energy and atomic force minimization.

The adsorption behavior of H_2O within MoS_2 layers was investigated by placing a MoS_2 layer, either pristine or with a specific type of vacancy defect, on top of another layer with adsorbed H_2O that has the same vacancy defects, using the most stable bilayer configurations, namely, AA′, AB, and AB′.[47,48] The initial bilayer interfaces were constructed by positioning the top MoS_2 layer 6.4 Å from the underlying layer, with this distance being the average layer spacing calculated from the Mo atoms in both layers. To account for the effects of the interactions between vacancy defects in adjacent layers and their effect on the H_2O adsorption at MoS_2 interfaces, two were aligned as close as possible to each other, with periodic replicas separated by a 15 Å vacuum perpendicular to the basal plane. The adsorption energy (Ea) for H_2O adsorbed on MoS_2 both for a
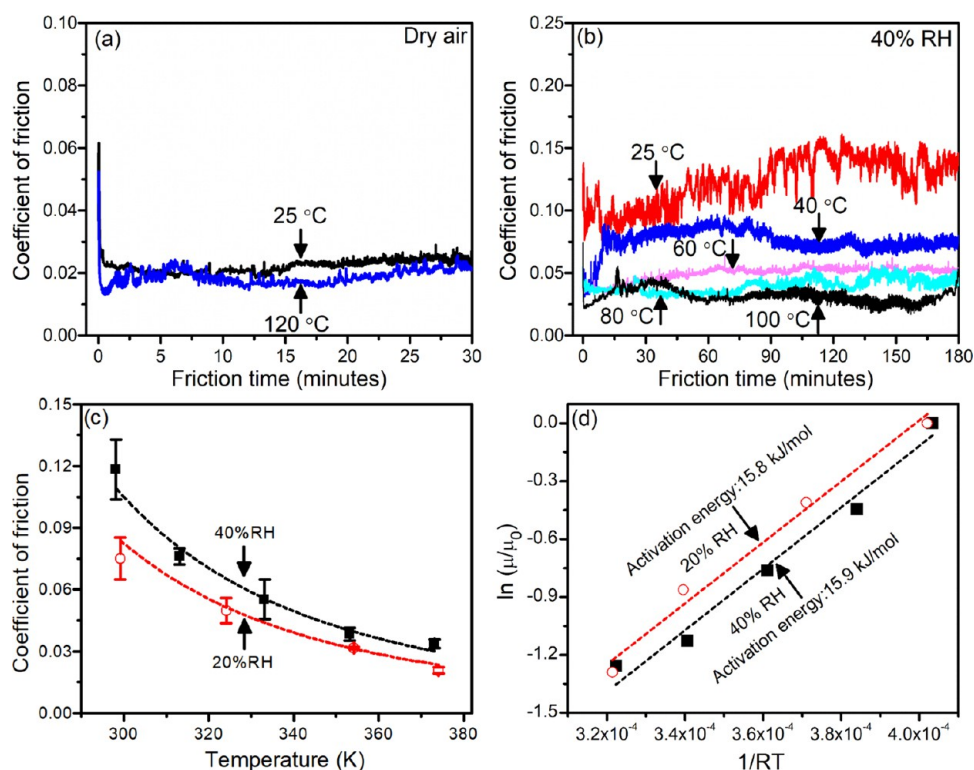
Figure 2. Coefficient of friction (COF) of the MoS$_2$ film (a) measured in dry air at 25 and 120 °C, (b) measured in a humid environment with 40% RH at 25, 40, 60, 80, and 100 °C. (c) Average COF at 25 °C (298 K), 40 °C (313 K), 60 °C (333 K), 80 °C (353 K), and 100 °C (373 K) measured under 40% RH and average COF measured under 20% RH at 25, 50, 80, and 100 °C and (d) linear fit of the COF plotted against temperature from (c) where R is the gas constant and μ and μ_0 are the average COF at the test temperature and at the baseline temperature of 25 °C (298 K), respectively. The slopes of the lines are consistent and represent the activation energy needed to break bonds or overcome energy barriers created by surface interactions.

monolayer and within the bilayers was calculated using the equation $E_a = E_{MoS_2 + H_2O} - E_{MoS_2} - E_{H_2O}$, where $E_{MoS_2 + H_2O}$ represents the total energy of the system with the adsorbed H_2O, E_{MoS_2} is the total energy of the MoS$_2$ layer (either monolayer or bilayer), and E_{H_2O} is the total energy of the isolated H_2O molecule, all calculated within the same simulation cell and using the same methodology.

To evaluate effect of the intercalated H_2O on the interfacial properties, the interlayer binding energy (E_B) was calculated using $E_B = (E_{layer1} + E_{layer2} + E_{H_2O} - E_{interface})/A$, where E_{layer1} and E_{layer2} are the total energies of isolated MoS$_2$ layers, E_{H_2O} is the total energy of the isolated H_2O molecule, $E_{interface}$ represents the total energy of the MoS$_2$ interface-intercalated H_2O, and A is the interfacial area. The E_B value for bilayer MoS$_2$ without intercalated H_2O was also calculated for comparison, where E_{H_2O} was taken as zero. To correlate changes in E_B with the friction behavior, interlayer sliding of MoS$_2$ layers with and without H_2O sandwiched between the bilayer MoS$_2$ interfaces was simulated by shifting the top MoS$_2$ layer over the underlying MoS$_2$ layer along the lattice X direction and in a direction normal to X by increments of 0.21 Å (see Figure S2). During the layer shifting simulations, the atoms in the bottom sulfur (S) layer of the lower MoS$_2$ layer were fixed in all directions, while the atoms in the top S layer of the upper MoS$_2$ layer were fixed laterally, allowing for out-of-plane movement.

3. RESULTS AND DISCUSSION

3.1. Experimental Observations of COF Values of MoS$_2$ in Humid Environments at Different Temperatures.
Starting with thermogravimetric (TG) and differential thermogravimetric (DTG) analyses of both pristine and ball-milled MoS$_2$ powders, insights into MoS$_2$'s thermal properties

are obtained, laying the foundation for subsequent sliding experiments in humid environments. As shown in the TG and DTG analyses of pristine MoS$_2$ and ball-milled MoS$_2$ powder presented in Figure S3, the pristine MoS$_2$ powder showed a minor weight loss (<0.2%) due to environmental water adsorption, with significant weight loss initiating at 395 °C and peaking at 480 °C—and totaling 7.8% by 600 °C. This showed that pristine MoS$_2$ adsorbs minimal water from the environment and remains structurally stable below 395 °C. In contrast, the ball-milled MoS$_2$ exhibited a marked weight loss of 4.7% below 150 °C, with the most rapid water desorption occurring between 40 and 100 °C. The ball-milled MoS$_2$ began to lose weight substantially starting from 250 °C, with DTG curves showing two deep valleys corresponding to rapid weight losses at temperatures of 300 and 450 °C as shown in Figure S3. Interestingly, the milled MoS$_2$ experienced a considerable weight loss of 25.4% at 100 °C. This significant weight loss can be attributed to both the initial mixing of MoS$_2$ with 10% H_2O and an oxidation process promoted by defects that facilitated the conversion of MoS$_2$ to both MoO$_2$ and MoO$_3$, with MoO$_2$ acting as an intermediate phase.[29,49,50] The transformation of MoS$_2$ into MoO$_2$ and MoO$_3$ would result in weight losses of 20 and 10% in atomic ratios, respectively.

Sliding tests were systematically conducted at temperatures ranging from 40 to 100 °C, a temperature range where significant H_2O desorption occurs. For comparative purposes, additional tests were performed at room temperature. Initially, sliding tests were performed in dry air both at 25 °C and at 120 °C to study the effects of oxidation and possible film softening on the COF. As shown in Figure 2a, the COF values of 0.022

at 25 °C and 0.019 at 120 °C in dry air were both low and closely matched, indicating that oxidation of MoS_2 or softening of the MoS_2 layers had a negligible effect on the COF. For these reasons, the effects of molecular adsorption and desorption on the friction of MoS_2 were studied by performing the sliding tests in a humid environment with 40% RH at the temperature range specified above, where the adsorbed H_2O molecules would be expected to gradually desorb from the adsorption sites with increasing temperature. As shown in Figure 2b, the MoS_2 exhibited an average COF of 0.12 at 25 °C under 40% RH, where the COF increased from the 0.10 at the beginning of the test to 0.13 at its conclusion. The increase in the COF toward the end of the testing period could be attributed to the accumulation of H_2O on the MoS_2 layers as H_2O is known to form a thin layer above 40% RH.[51−53] It should be noted that prior to testing, the initial MoS_2 film was preconditioned by baking at 100 °C for a minimum of 1 h to remove surface H_2O. As the sliding test temperature increased, the average COF decreased steadily to 0. 076 at 40 °C, 0.049 at 60 °C, 0.037 at 80 °C, and 0.032 at 100 °C. It is interesting to note that the most significant reduction in the COF was observed within the narrow temperature range between 25 and 40 °C, a trend consistent with the thermogravimetric (DGT) analysis, which indicated a high H_2O desorption rate within this temperature range. Moreover, the COF at 100 °C remained higher at 0.032 than the value recorded in dry conditions, suggesting that H_2O adsorption still impacts the friction of MoS_2 at this elevated temperature.

The average COF from three repeated tests (one example of which is depicted in Figure 2b) is plotted in Figure 2c, illustrating the decrease in the COF with an increase in temperature, with temperature measured in Kelvin on the abscissa. A logarithmic plot of the data in Figure 2c is presented in Figure 2d, where μ represents the COF at different temperatures and μ_0 is the COF at 25 °C, with R and T as the gas constant and the temperature, respectively. A linear fit of the normalized friction $(\ln(\mu/\mu_0))$ against the inverse of temperature $(1/RT)$ showed a slope corresponding to an activation energy (E_A) of 15.9 kJ/mol or 0.165 eV. To support these findings, tests were also conducted under 20% RH, and the results are plotted in Figure 2c (for the corresponding friction curves, refer to Figure S4). These tests revealed a similar reduction in friction at both humidity levels with increasing temperature. Notably, almost the same slope was observed for tests conducted under 20% RH, indicating an E_A of 15.8 kJ/mol or 0.164 eV, as depicted in Figure 2d. The similar E_A values observed at both 20 and 40% RH levels suggest that the underlying process governing the COF in these cases is likely the same. Consequently, these results further substantiate the influence of humidity on friction, primarily attributable to the adsorption of water molecules at defect sites. This phenomenon affects the COF but does not markedly alter the activation energy required for sliding between the surfaces within the tested humidity range. It is worth noting that the E_A determined in Figure 2d is almost the same as that of 16 kJ/mol[54] obtained from tests of sliding borosilicate glass over a carbon nanotube under 45% RH, indicating the same friction mechanism operating at different friction interfaces. Meanwhile, the E_A is slightly lower than the activation energy barrier of 0.3 eV, as reported in a previous study.[55] In that study, the barrier was attributed to an analogy with the activated propagation of dislocations during the microscopic friction analysis at various temperatures for sliding

a Si_3N_4 tip against MoS_2. Considering the athermal behavior of MoS_2, which exhibits a consistent COF of 0.02 at both 25 and 120 °C in a dry air environment (as shown in Figure 2a), the obtained E_A in Figure 2d likely corresponds to energy required for reducing interfacial bonds via thermal desorption of H_2O molecules from MoS_2 surfaces. As the energy required to desorb molecules from surfaces is generally at the same level as their corresponding adsorption energy (Ea), the E_A value aligns with Ea in the range of −0.16 to −0.28 eV[56,57] previously calculated for H_2O adsorption at V_{Mo}, V_S, and V_{S2} sites of MoS_2 using first-principles computations.

The morphologies of the worn surfaces were first examined using SEM-EDS. According to Figure 3, material transfer from the MoS_2 film to the ball surfaces was observed for all tests
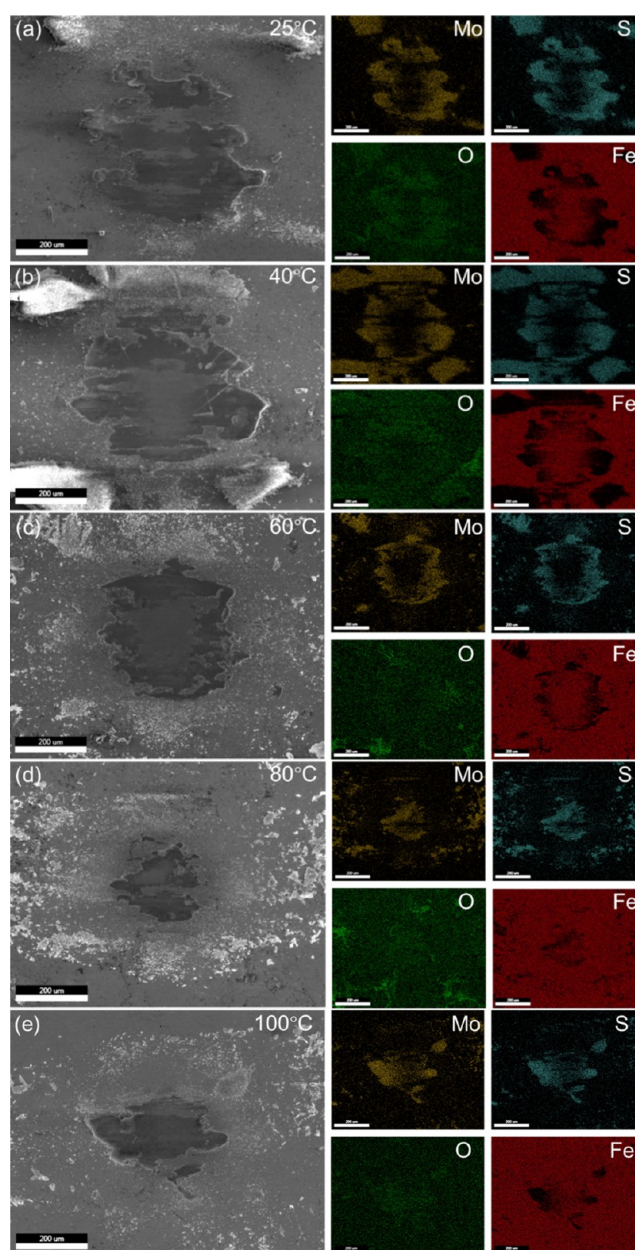
Figure 3. SEM images and EDS maps of the 52100 steel ball surface slid against MoS_2 under 40% RH illustrating morphological and compositional changes at temperatures of 25 °C (a), 40 °C (b), 60 °C (c), 80 °C (d), and 100 °C (e).
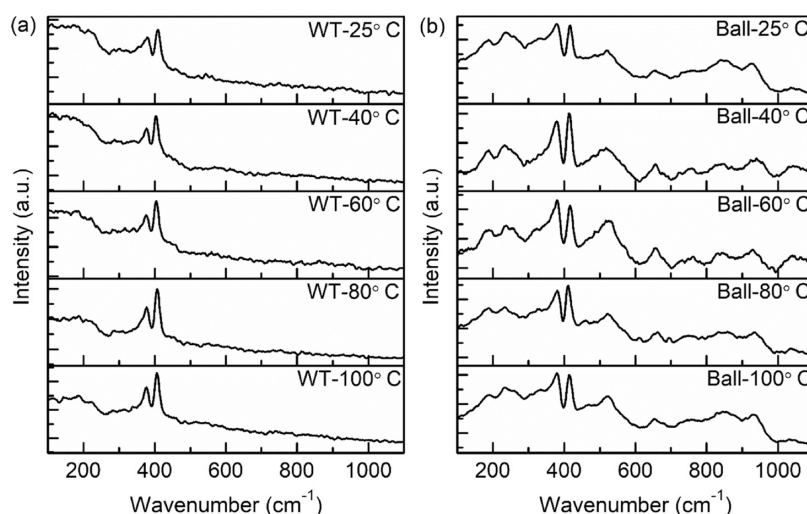
Figure 4. Raman spectra obtained from wear tracks (a) and ball surfaces (b) tested at temperatures of 25 °C, 40 °C, 60 °C, 80 °C, and 100 °C under 40% RH.
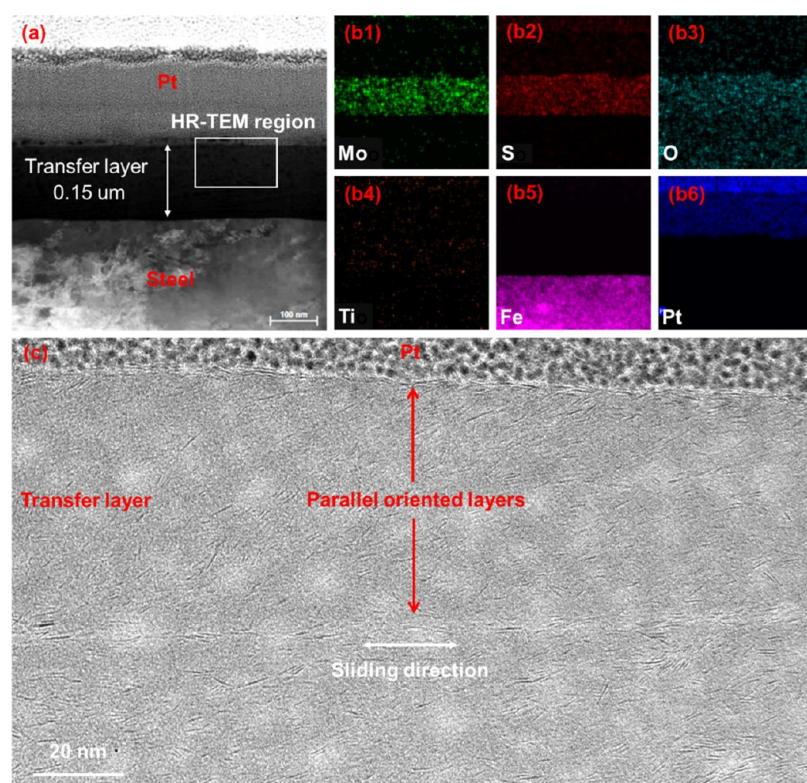

Figure 5. (a) Low-magnification cross-sectional TEM image of the transfer layer formed on the AISI 52100 steel ball surface slid against MoS_2 under 40% RH at 25 °C. (b) EDS elemental maps of (a) showing distributions of Mo (b1), S (b2), O (b3), Ti (b4), Fe (b5), and Pt (b6). (c) HR-TEM image taken from the boxed region in (a).

performed across the temperature range of 25 to 100 °C, conducted at a constant 40% RH. It is also noted that the diameter of the wear scars on the ball surface decreased with increasing temperatures, corresponding with the COF reduction trends as shown in Figure 2. Meanwhile, SEM analysis indicated that the wear tracks on the MoS_2 displayed minimal wear, with a negligible transfer of material from the steel counterface. A representative SEM-EDS mapping of the wear track of MoS_2 tested at 25 °C displayed in Figure S5 predominantly showed signals of Mo and S with traces of O in the debris accumulated at the edge of the wear track indicative

of minimal oxidative wear. The Raman spectroscopy of the wear tracks of MoS_2 shown in Figure 3a further confirmed the persistence of MoS_2 in the wear tracks after testing under varied temperatures. The micro-Raman spectroscopy in Figure 4a confirmed that the wear tracks consisted of MoS_2, which did not oxidize significantly during sliding. The identification of similar Raman peaks on the transfer layers formed on the ball surfaces confirmed that MoS_2 was transferred to the counterface and formed MoS_2-rich zones.

FIB-TEM analyses were performed to assess structural changes during the sliding process and to clarify how H_2O
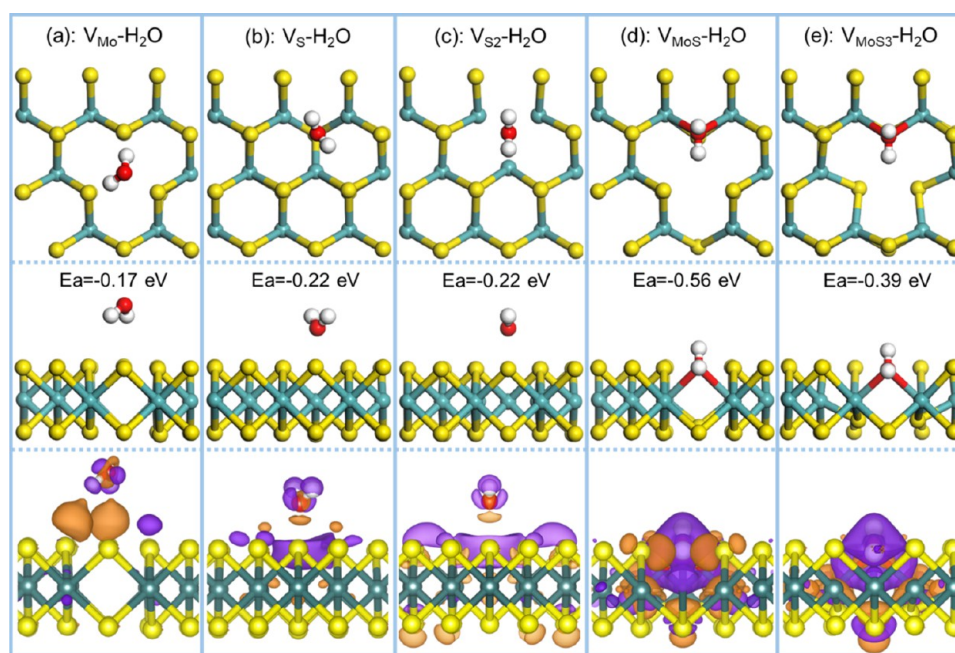
Figure 6. Top (first row) and side (second row) views of H_2O molecule adsorption configurations at vacancy sites of monolayer MoS_2. The specific sites are (a) molybdenum vacancy V_{MO}, (b) at a sulfur vacancy V_S, (c) at a disulfur vacancy V_{S2}, (d) at a site with a missing molybdenum and adjacent sulfur V_{MoS}, and (e) at a site with a missing molybdenum and three sulfurs V_{MoS3}. The corresponding charge density difference (CDD) contours are depicted in the bottom row, illustrating regions of electron depletion (orange) and accumulation (purple), which are indicative of changes in the electronic structure due to adsorption. The adsorption energy (Ea) values are marked on the diagram range from −0.17 to −0.56 eV with V_{MoS} showing the strongest adsorption affinity. Isosurface levels for CDD contours are set at 0.0005 e/Bohr^3 for (a−c) and 0.002 e/Bohr^3 for (d, e).

molecules affected the layered structures. As shown in Figure 5a, a low-magnification cross-sectional TEM image acquired from the counterface surface after sliding contact with MoS_2 revealed the formation of an approximately 0.15 μm-thick layer. The elemental EDS maps presented in Figure 5b showed that the transfer layer consisted mainly of Mo and S, with a trace presence of O, which could have been integrated during the sliding process in the humid environment. A small quantity of Ti was also observed, which could be attributed to the incidental transfer from the interlayer within the MoS_2 coating structure. The HR-TEM image of the transfer layer taken from the boxed area in Figure 5a is presented in Figure 5c. In contrast to the structure of as-deposited MoS_2 in Figure 1, the initially misoriented MoS_2 layers were reoriented along the sliding direction. This realignment was particularly pronounced at the top of the transfer layer, which was in direct sliding contact and extended 3−5 layers of MoS_2. These TEM observations were consistent with our previous TEM observations.[29,58] Thus, while the MoS_2 transfer layer provided a low-friction MoS_2/MoS_2 interface, these parallel layers formed under humid conditions did not result in as low a friction as observed in a dry environment.

According to the experimental observations, it can be suggested that parallel MoS_2 layers could be formed during the sliding process, and oxidation of the MoS_2 during tests in a humid environment was insignificant as supported by the Raman, SEM, and TEM analyses. However, the friction was obviously affected by H_2O molecules from the testing environment. The normalized COF showed a decreasing trend with increasing temperature that obeyed the Arrhenius equation, providing an activation energy of 0.165 eV for the friction process, which could be related to the activation energy required to desorb the H_2O molecule from MoS_2. Thus, the

experimental analyses indicate that the increased friction of MoS_2 in a humid environment was likely due to the H_2O adsorption behavior that significantly hinders MoS_2 layer sliding. Accordingly, in the following sections, density functional theory (DFT)-based first-principles calculations are presented. DFT studies aimed at a deeper understanding of the thermodynamics of H_2O physisorption on MoS_2. Eventually, these calculations shed light on how the adsorption contributes to an increase in layer shear resistance and, consequently, to the observed increase in friction.

3.2. H_2O Adsorption at Defects of MoS_2: Adsorption Energy, Charge Transfer, and DOS Analyses. The adsorption behavior of H_2O at V_S, V_{S2}, V_{Mo}, V_{MoS}, and V_{MoS3} was investigated by calculating their adsorption energies. In previous studies, such as ref 29, it was observed that water molecules showed a tendency to dissociate when adsorbed at the V_{MoS2} site. The current study, however, does not observe this dissociative behavior at other types of defects (V_S, V_{S2}, V_{Mo}, V_{MoS}, and V_{MoS3}), even when the water molecule is placed in close proximity to the sulfur layer (0 or 2 Å above it). This suggests that these smaller and less reactive defects do not facilitate the same chemical reactions as the V_{MoS2} site.

The absence of dissociation at these vacancy sites implies that water molecules are likely to remain intact (physisorbed) rather than breaking apart and reacting with the surface atoms. This is supported by the exothermic nature of the adsorption process, as indicated by the calculated activation energy (Ea) values for each type of vacancy, namely −0.17 eV for V_{Mo}, −0.22 eV for V_S and V_{S2}, − 0.56 eV for V_{MoS}, and −0.39 eV for V_{MoS3}. When compared to the pristine MoS_2 layer with a relatively high Ea of −0.15 eV,[33] these vacancies promoted H_2O adsorption on MoS_2, and the adsorption configurations are thermodynamically stable.

The adsorption behavior of H_2O molecules on various vacancy defects in MoS_2 was investigated. H_2O showed different orientations and bonding characteristics at different defect sites. As shown in Figure 6, both top and side views indicated that the H_2O adsorption on V_S and V_{S2} results in nearly identical configurations with the O atom from H_2O positioned above the vacant S defects. The distance to the S plane measures 1.92 Å for V_S and 1.98 Å for V_{S2}. As for the H_2O orientation on the V_{Mo} site, it can be seen from Figure 6c that the H_2O molecule undergoes a significant change from its initial configuration (H_2O parallel to the MoS_2 basal plane as illustrated in Figure S2). In this new configuration, its two H atoms are oriented toward two adjacent S atoms with a distance of 2.79 Å. The molecule is situated farther from the S plane, with a distance of 2.57 Å. Compared to large separations observed between H_2O and the V_S, V_{S2}, and V_{Mo} sites on MoS_2, the H_2O was adsorbed directly within the S plane of MoS_2 at the V_{MoS} and V_{MoS3} sites, exhibiting nearly identical orientations. In this configuration, one −OH group of H_2O was adsorbed within the S plane, forming Mo−O−Mo bonds with bond lengths measuring 2.46 Å for V_{MoS} and 2.53 Å for V_{MoS3}. The shorter Mo−O−Mo bonds at V_{MoS} may contribute to the lower Ea value. It should be noted that the Mo−O bond length can vary within the range of 1.68−2.53 Å depending on the bond coordination.[59] In the case of H_2O adsorption at the V_{MoS} site, the Mo−O−Mo bond length is higher than the value of 2.34 Å for undissociative H_2O adsorption at V_{MoS2} and significantly larger than the 2.10 Å length (with an Ea of −1.22 eV) recorded for dissociative H_2O adsorption at V_{MoS2}.[29] Thus, considering the activation energy and formation of new bonds at the vacancy sites, the reactivity of vacancy defects of MoS_2 to the H_2O molecule can be ranked as follows: $V_{MoS2} > V_{MoS} > V_{MoS3} > V_{S2}(V_S) > V_{Mo}$.

Each type of vacancies would provide an unique bonding environment for molecule adsorption, leading to distinct charge redistribution and behavior during the adsorption process. For this reason, the charge density difference (CDD) analyses were performed to understand the electronic interactions between H_2O and MoS_2 at the vacancy defect sites. The CDD ($\Delta\rho$) was calculated using $\Delta\rho = \rho_{total} - \rho_{MoS_2} - \rho_{H_2O}$, where ρ_{total}, ρ_{MoS_2}, and ρ_{H_2O} represent the charge density of MoS_2 with H_2O, MoS_2 alone, and H_2O alone, respectively. The isosurface contour was visualized using VESTA.[60] As can be seen from the bottom row in Figure 6a−c, it is evident that different degrees of charge accumulation occur around the H_2O molecule at the V_{Mo}, V_S, and V_{S2} sites of MoS_2 when the isosurface contours were plotted in an isosurface value set to 0.0005 e/Bhor³. It can be noted that at the V_{Mo} vacancy, the two −OH groups induced directional charge accumulation originating from the two adjacent S atoms. Meanwhile, the charge transfer behavior for H_2O adsorption at V_S and V_{S2} sites showed similar charge accumulation zones (as indicated by the purple color at the bottom row of Figure 6b,c) at the center of the vacancy site where dangling Mo bonds are present. Additionally, charge depletion zones near the O atom of H_2O can be identified by the orange color on the charts. It is interesting to note the differences in charge accumulation zones in Figure 6b,c, particularly in the areas that coincide with the occurrence of charge depletion zones near the S atoms from the bottom S layer near the VS_2 site of MoS_2. However, when compared to the charge transfer behavior for H_2O adsorbed at the V_{MoS} and

V_{MoS3} sites as shown in Figure 6d,e, the charge transfer zones observed in Figure 6a−c were barely discernible when the charge density contours were plotted using the same isosurface value.

The charge transfer behaviors between H_2O and MoS_2 at V_{MoS} and V_{MoS3} were similar to each other, except that there was an occurrence of charge depletion zones originating from two adjacent S atoms at the vacancy sites, indicating an in-plane interaction between the −OH and the S atoms within the MoS_2 plane. This in-plane interaction would result in a more stable adsorption state as evidenced by the lower Ea value of −0.56 eV. Therefore, the CDD analyses revealed a stronger interaction between H_2O and MoS_2, with more significant charge transfer occurring at V_{MoS} and V_{MoS3} sites. These results agree with the computed Ea values mentioned above.

To quantify the electron transfer between the H_2O molecule and MoS_2 at five different vacancy sites, the Bader charge analysis[61−63] was employed. This method approximates the charge state of each atom involved. The net charge on atom (Q_{net}) is calculated as $Q_{net} = Q_{Bader} - Q_{valence}$, where Q_{Bader} is the calculated Bader charge and $Q_{valence}$ is the number of pseudoelectrons of each element (6 for O and 1 for H). The change in the total number of electrons after adsorption on MoS_2 is calculated using $\Delta Q_{H_2O} = Q_{H_2O\text{-ads}} - Q_{H_2O\text{-iso}}$ with $Q_{H_2O\text{-ads}}$ and $Q_{H_2O\text{-iso}}$ representing Bader charge of H_2O adsorbed on MoS_2 and isolated H_2O, respectively. This calculation provides insights into the electron transfer dynamics during the adsorption process. As shown in Table S1, the charge distributions for an isolated H_2O molecule agree well with previous simulation work.[63] For the H_2O adsorption configurations that exhibited higher Ea values, namely V_{Mo}-H_2O, V_S-H_2O, and V_{S2}-H_2O, there was minimal net charge transfer to the H atoms with Q_H values comparable to those of isolated H_2O, whereas a slightly reduced charge on the O atom was observed for V_{Mo}-H_2O and V_S-H_2O. In contrast, H_2O molecules adsorbed at the more reactive V_{MoS}, V_{MoS2}, and V_{MoS3} sites, which corresponded to lower Ea values, showed a significant redistribution of net charges. Notably, there was a considerable charge accumulation on H_1 (ranging from −0.607 to −0.635 e), attributed to the shorter H−S distance (with H_1 adsorbed in the S plane), and a less pronounced charge transfer on H_2. These variations in charge transfer patterns are also evident in the CDD contours shown in Figure 6d,e.

On the other hand, the charge transfer of the O atom from the H_2O molecule depends on the type of vacancy defects. The O atom showed almost the same charge transfer (1.151 e) at the V_{MoS3} site but had an increased charge transfer at V_{MoS} (1.194 e) and V_{MoS2} (1. 212 e) sites. Here, in addition to a dissociated H_2O, a second undissociated H_2O adsorbed at the V_{MoS2} site was used to estimate the charge transfer behavior between H_2O and MoS_2 at the vacancy defect site.[29] The total charge transfer of the H_2O molecule indicates that H_2O gained electrons (0.013−0.018 e) when absorbed at V_{Mo}, V_S, and V_{S2} sites but lost electron to MoS_2 (0.021−0.034 e) when adsorbed at more reactive V_{MoS}, V_{MoS2}, and V_{MoS3} sites. This electron loss is associated with the formation of the Mo−O−Mo bond with a relatively larger bond length of ∼2.5 Å, indicating a substantial chemical interaction. These charge transfer analyses agree well with the Ea values of H_2O at different types of vacancy above. This correlation indicates that an increase in electron transfer from the H_2O molecule to

Table 1. Interlayer Spacing d, Binding Energy E_B, and Adsorption Energy Ea Values for Bilayer MoS$_2$ Interfaces with and without Adsorbed H$_2$O Molecules

MoS$_2$ bilayer interfaces	AA′			AB			AB′		
	d (Å)	E_B (J/m^2)	Ea (eV)	d (Å)	E_B (J/m^2)	Ea (eV)	d (Å)	E_B (J/m^2)	Ea (eV)
V$_S$/pristine	6.44	0.30		6.40	0.30		6.43	0.29	
V$_{MoS}$/pristine	6.43	0.30		6.41	0.30		6.45	0.30	
V$_{MoS3}$/pristine	6.43	0.28		6.41	0.28		6.41	0.27	
V$_S$/V$_S$	6.41	0.29		6.40	0.30		6.40	0.29	
V$_{MoS}$/V$_{MoS}$	6.41	0.30		6.38	0.30		6.38	0.30	
V$_{MoS3}$/V$_{MoS3}$	6.43	0.25		6.39	0.25		6.42	0.25	
V$_S$-H$_2$O/pristine	6.52	0.30	0.01	6.52	0.29	0.11	6.55	0.28	0.10
V$_{MoS}$-H$_2$O/pristine	6.42	0.37	−0.67	6.41	0.38	−0.67	6.42	0.37	−0.67
V$_{MoS3}$-H$_2$O/pristine	6.42	0.34	−0.57	6.40	0.34	−0.58	6.40	0.33	−0.55
V$_S$-H$_2$O/V$_S$	6.47	0.30	−0.01	6.44	0.30	−0.02	6.54	0.29	0.02
V$_{MoS}$-H$_2$O/V$_{MoS}$	6.40	0.38	−0.72	6.37	0.38	−0.74	6.37	0.37	−0.72
V$_{MoS3}$-H$_2$O/V$_{MoS3}$	6.40	0.31	−0.57	6.39	0.31	−0.55	6.38	0.31	−0.50
V$_{MoS}$-H$_2$O/H$_2$O−V$_{MoS}$	6.42	0.43	−1.19	6.38	0.45	−1.40	6.41	0.42	−1.20
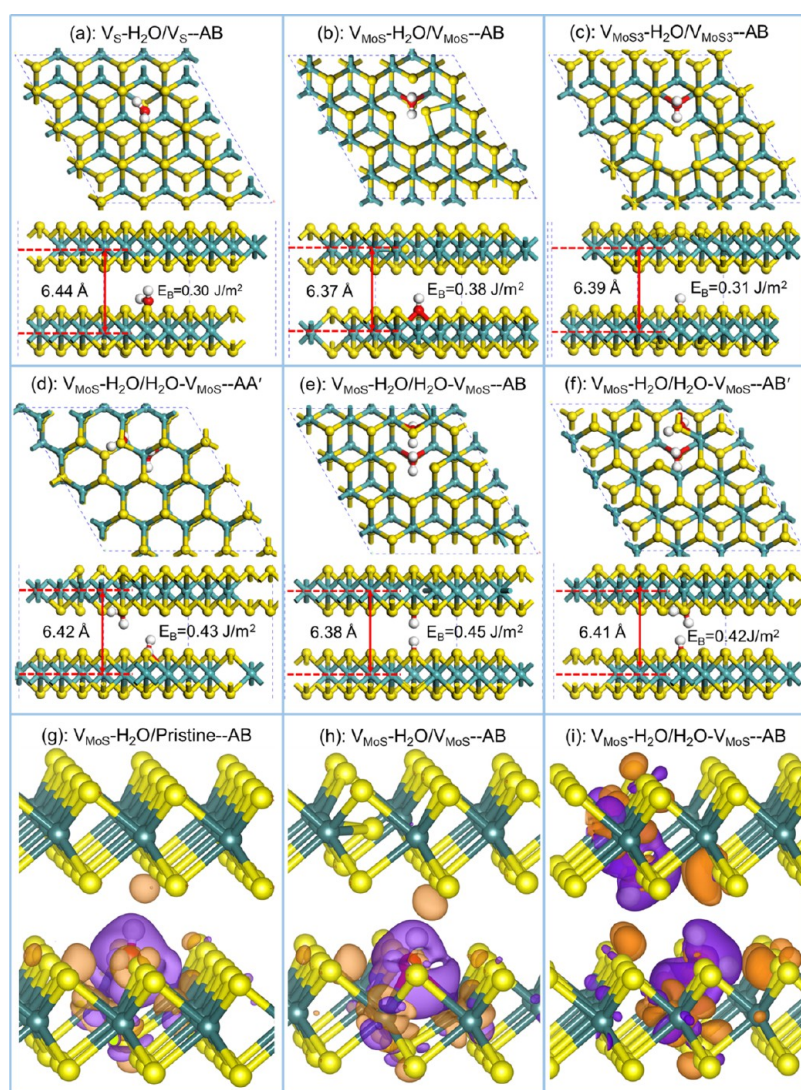
Figure 7. Bilayer MoS$_2$ interfaces with a single H$_2$O molecule in the AB stack for configurations of (a) V$_S$-H$_2$O/V$_S$, (b) V$_{MoS}$-H$_2$O/V$_{MoS}$, and (c) V$_{MoS3}$-H$_2$O/V$_{MoS3}$. Bilayer interfaces with two intercalated H$_2$O molecules in (d) AA′, (e) AB, and (f) AB′ stacking configurations of V$_{MoS}$-H$_2$O/ H$_2$O−V$_{MoS}$. CDD contours for AB stacked interfaces are shown for (g) V$_{MoS}$-H$_2$O/Pristine, (h) V$_{MoS}$-H$_2$O/V$_{MoS}$, and (i) V$_{MoS}$-H$_2$O/H$_2$O−V$_{MoS}$ configurations. The CDD contours are visualized with an isosurface value of 0.002 e/Bhor^3, where orange and purple indicate charge depletion and accumulation, respectively.

MoS_2 sites, as revealed by the charge analysis, aligns with a decrease in Ea, suggesting that stronger electron transfer corresponds to more energetically favorable adsorption.

Spin-polarized density of states (DOS) calculations for representative structures of H_2O adsorbed at V_{Mo}, V_S, and V_{MoS} sites on MoS_2 were conducted to understand the H_2O adsorption process at these defects. The results in Figure S6 show orbital hybridization between S-2p and Mo-4d due to the formation of Mo−S bonds, which is consistent with previous simulation work on DOS for V_S and $V_{Mo \ sites}$.[46] Notably, three midgap states were observed between 0 and 1 eV in the projected DOS (PDOS) of Mo and S in Figure S6(a), and two midgap states are located at the valence band edge and near 1 eV in Figure S6(b). Similar midgap states are also found in Figure S6(c) for V_{MoS}-H_2O. Compared to the DOS for H_2O adsorption at V_{Mo} and V_S, the V_{MoS}-H_2O system exhibited spin polarization, as evident from the difference between the spin-up and spin-down peaks, resulting in a net magnetic moment of 2 μB. This polarization was accompanied by an orbital hybridization between 2p states of H and O and 4d states of Mo as shown in the PDOS plots. Meanwhile, no such orbital hybridization between atoms from H_2O and MoS_2 was observed for adsorption at V_S and V_{Mo} sites. Thus, the strong orbital hybridization between O-2p and Mo-4d states, along with the formation of Mo−O−Mo bonds, significantly enhances H_2O adsorption on V_{MoS} sites, leading to the lowest Ea for the V_{MoS}-H_2O system.

3.3. H$_2$O Adsorption at MoS$_2$ Interfaces and Its Roles in Interfacial Bonding and Layer Sliding.

The presence of H_2O molecules between MoS_2 layers leads to changes in interlayer spacing and binding energy (E_B). To investigate the role of H_2O adsorption in the adhesion and sliding behavior of MoS_2 layers, bilayer MoS_2 interfaces were constructed. This was achieved by placing a pristine MoS_2 layer and a similarly vacancy-defected MoS_2 layer on top of the MoS_2 layers in configurations including V_S-H_2O, V_{MoS}-H_2O, and V_{MoS3}-H_2O. This arrangement ensured that only one H_2O molecule was positioned between the MoS_2 layers. The interfaces representing the most stable stacking sequences were used in order to estimate the effects of H_2O adsorption on interfacial bonding and structures. For comparison, the same interfaces without H_2O intercalation were also computed, as summarized in Table 1. As shown in Table 1, when examining the interfaces without H_2 intercalation, the binding energy (E_B) values quantifying the strength of the interlayer interaction or bonding between the two layers exhibited a similar range in the AA′, AB, and AB′ stackings. Notably, the AB stacking configuration displayed the smallest interlayer spacing among them. It can also be noted that a larger vacancy of V_{MoS3} on MoS_2 resulted in a reduction in the E_B from ∼0.30 to 0.25 J/m^2. This reduction can be attributed to the weakened interlayer interaction induced by the void created by the larger vacancy.

When examining the bilayer configurations intercalated with a H_2O molecule, it can be noted from Table 1 that the presence of H_2O did not alter the E_B value for the V_S/V_S and V_S-H_2O/pristine (unmodified) configurations across all the three computed stackings. However, there was an increase in the interlayer spacing by 0.04−0.14 Å. Additionally, the Ea values were found to be in the range of −0.02 to 0.11 eV, which were higher than Ea values for H_2O on pristine and V_S-defected monolayer MoS_2. This suggests the existence of a competition between the adsorption process, which lowers the

system's energy, and a process that increases the system's energy by weakening the van der Waals interaction due to the expanded layer spacing.

This phenomenon is demonstrated in Figure 7a and characterized by a significant expansion in the layer spacing, reaching 6.44 Å. This expansion occurred when the H_2O molecule was adsorbed onto the V_S site of MoS_2 from the underlying layer. For H_2O adsorbed at V_{MoS} and V_{MoS3} sites, the H_2O intercalated at the interfaces increased the E_B values to 0.31−0.37 J/m^2 without increasing the interlayer spacing (see Figure 7b,c). Moreover, H_2O was more likely to be adsorbed at these interfaces due to the low Ea values of −0.50 to −0.74 eV. Compared to the interfaces with pristine (defect-free) top layer MoS_2, Table 1 shows that the interlayer spacings for interfaces with vacancies in both MoS_2 were 0.01−0.08 Å smaller. Also, it was observed that H_2O was most stably adsorbed at interfaces containing the V_{MoS} defect.

To understand how E_B and layer spacing would change with an increased number of intercalated H_2O molecules, interfaces of V_{MoS}-H_2O/H_2O−V_{MoS} with both layers containing the V_{MoS} defect and each adsorbed with a H_2O molecule were constructed in AA′, AB, and AB′ stackings and then simulated. According to the computed structures shown in Figure 7d,e, the AB stacking configuration, which had the smallest layer spacing of 6.38 Å, showed the highest E_B of 0.45 J/m^2. This was followed by 0.43 J/m^2 in the AA′ stack and 0.42 J/m^2 in the AB′ stack, the latter having a slightly larger layer spacing. Moreover, the Ea values were −1.19, − 1.40, and −1.20 eV for V_{MoS}-H_2O/H_2O−V_{MoS} in AA′, AB, and AB′ stackings, respectively. These values were approximately double those for interfaces with only one intercalated H_2O molecule. Hence, the computational data suggested that increased H_2O adsorption at the interface led to higher E_B values.

CDD studies were conducted to illustrate the changes in electronic properties in the presence of intercalated H_2O molecules. Charge transfer isosurface contour plots, as a tool in CDD analysis, were utilized to illustrate these changes. Figure 7g−i shows typical contour plots for V_{MoS}-H_2O/Pristine, V_{MoS}-H_2O/V_{MoS}, and V_{MoS}-H_2O/H_2O−V_{MoS} configurations in the AB stacking, respectively. The charge depletion zone (indicated by the orange zone) from the S atom of the top MoS_2 layer for V_{MoS}-H_2O/V_{MoS} in Figure 7h was larger than that in Figure 7g for V_{MoS}-H_2O/Pristine, which agrees well with the lower Ea value of −0.74 eV for the former compared to −0.67 eV for the latter. Thus, the V_{MoS} defect enhanced H_2O adsorption to both the upper and lower MoS_2 layers. Compared to the configurations with a single H_2O molecule intercalated at the interfaces, the V_{MoS}-H_2O/H_2O−V_{MoS} configuration with two H_2O molecules adsorbed at the interface as shown in Figure 7i exhibited more significant charge transfer as evidenced by two orange zones near S atoms of both layers. This correlates with the lowest Ea of −1.40 eV for the configurations with two intercalated H_2O molecules.

The CDD analyses revealed that the Ea values for H_2O adsorption on monolayer MoS_2 represent the interaction energy between the H_2O molecule and the MoS_2 layer. However, for H_2O adsorbed at bilayer interfaces, the Ea values reflect the change in the system's energy due to H_2O forming bonds with both the top and bottom MoS_2 layers. These interfacial bonds are likely characterized by H···S hydrogen bonds, with a bond length of ∼2.7 Å. These results indicated that an increased number of H_2O molecules adsorbed at the MoS_2 interface lead to stronger interlayer adhesion, resulting in
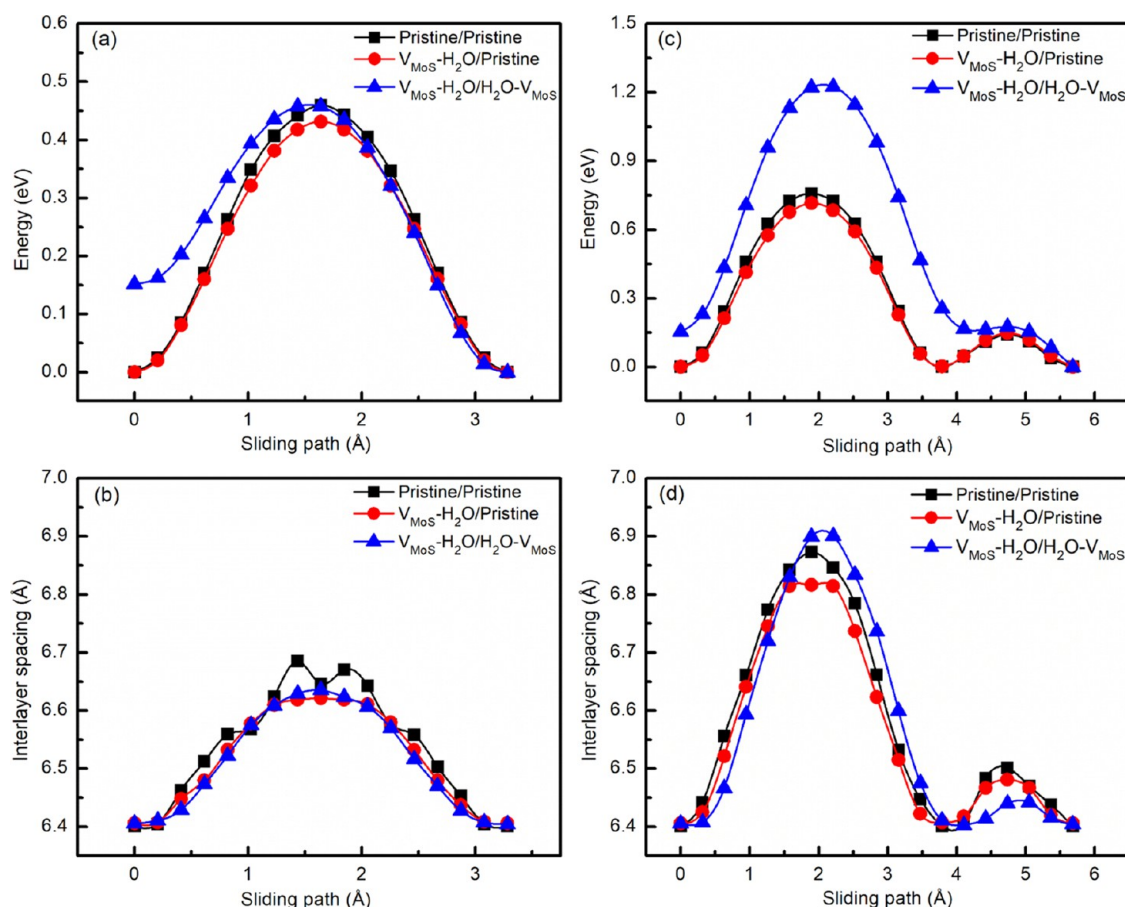
Figure 8. Energy variation and interlayer spacing of bilayer MoS_2 with and without an intercalated H_2O molecule during sliding motion in (a,b) in the X direction and (c, d) in the Y direction (refer to Figure S2 for X and Y direction orientations).

MoS_2 layers being interconnected by hydrogen bonds, which would impede layer shearing during the sliding process.

At this point of the discussion, it is appropriate to highlight some noteworthy aspects related to the E_B calculations. Due to the difference in vacancy properties, dissociation occurs only at V_{MoS2}, while physisorption is observed at all types of vacancies. The current computational study expands on previous findings 29 by illustrating that H···S hydrogen bonds can form at vacancies other than V_{MoS2}. This further supports the notion that water adsorption at defects can elevate friction, with this effect being reversible with temperature changes. Second, regarding the calculation of E_B, it is important to note that using the conventional formula might overestimate layer adhesion. This overestimation occurs because the H_2O adsorption energy to both the upper and lower layers is considered simultaneously. Practically, during layer separation, H_2O is expected to detach from the weakest adsorption sites, such as by breaking the H···S bond at the interface. Despite this, the trend and values of E_B still provide valuable insights into the frictional properties of MoS_2 in moist environments, notably indicating an increase in friction.

To rationalize the effect of H_2O molecules on the sliding behavior of the MoS_2 layer, a DFT study was undertaken. This approach is particularly valuable as direct experimental observation of this process, such as using atomic force microscopy, is challenging due to the complexity of the system.

3.4. Sliding Behavior of MoS_2 Layers with Adsorbed H_2O Molecules. DFT studies were performed to shed light on the effects of H_2O adsorption at MoS_2 interfaces on the

interlayer sliding behavior in three AB stacked bilayer MoS_2 configurations, namely (1) Pristine/Pristine, (2) V_{MoS}-H_2O/Pristine, and (3) V_{MoS}-H_2O/H_2O−V_{MoS}. Layer sliding in the X and Y directions (normal to X) was considered. When sliding along the Y direction, the H_2O molecule adsorbed on the top MoS_2 layer remains positioned above the H_2O molecule adsorbed on the underlying MoS_2 layer. However, this arrangement does not apply when sliding along the X direction.

The changes in the system energy and interlayer spacings during sliding the MoS_2 are presented in Figure 8a−d. According to Figure 8a,b, when sliding along the X direction for the three interfaces, it is evident that the presence of H_2O at the interfaces does not significantly alter the interlayer sliding energy barrier (0.43 eV for V_{MoS}-H_2O/Pristine and 0.46 eV for the other two interfaces). The variations in the interlayer spacing showed similar trends with those observed in the interlayer sliding energy. This behavior could be related to the relatively longer H···S bond length, which facilitates hydrogen bonding between adjacent S atoms. This can be inferred from the relatively smaller interlayer spacing observed in V_{MoS}-H_2O/Pristine and V_{MoS}-H_2O/H_2O−V_{MoS} compared to that of Pristine/Pristine (see Figure 8b). The results for sliding along the Y direction in Figure 8c,d showed a significant change in the interlayer sliding energy barrier due to the presence of H_2O at the interfaces. Specifically, the energy barrier was 0.72 eV for V_{MoS}-H_2O/Pristine, 0.76 eV for Pristine/Pristine, and 1.23 eV for V_{MoS}-H_2O/H_2O−V_{MoS}. The maximum energy barrier for pristine MoS_2 layers in an AB

stack sliding along the Y direction, which was 0.76 eV, agrees well with previous simulation results of 0.88 eV (scaled to a 4 × 4 cell) using the PBE + D potential.[64]

Thus, the presence of H_2O at the interfaces typically increased the interlayer sliding energy barrier when sliding along the Y direction. Although shifting along the Y direction resulted in a higher sliding energy barrier and larger interlayer spacing (6.8–6.9 Å), the sliding behavior of V_{MoS}-H_2O/ Pristine with a lower interlayer spacing and sliding energy barrier than those of Pristine/Pristine also suggests that H_2O at the interface suppressed layer expansion induced by repulsion between S planes at the energy barrier position. Meanwhile, considering the energy barrier position, the repulsion between the upper and lower layers was intensified by the repulsion between the two intercalated H_2O molecules. This effect is evident from the increased interlayer spacing, reaching a maximum of 6.9 Å for the V_{MoS}-H_2O/H_2O−V_{MoS} configuration as shown in Figure 8d. The water molecules tend to repel each other and consequently increase the layer spacing. Meanwhile, when the H_2O molecule slides against the S plane, the formation of H⋯S hydrogen bonds acts as a spring-like bond, restraining the increase in the layer spacing as the interface transitions from a close-layered stacking to one with greater layer separation. Consequently, this process leads to a significantly higher sliding energy barrier, peaking at 1.23 eV.

MoS_2 layers without an intercalated H_2O molecule were bonded primarily through the van der Waals interaction between negatively charged S layers, which ensured a low friction of 0.02 for sliding MoS_2 in dry air at both 25 and 120 °C as shown in Figure 2a. When a H_2O molecule was adsorbed at the MoS_2 interface as presented in Table 1 without increasing the layer spacing, H⋯S hydrogen bonds would form between the positively charged hydrogen from H_2O and the negatively charged S atom from the adjacent MoS_2 layer, alongside van der Waals interactions. These hydrogen bonds would enhance the interfacial adhesion, which in turn restricts layer expansion and consequently impedes layer sliding. Given that hydrogen bonding is stronger than van der Waals interactions and considering that defect structures, which promote H_2O adsorption, can inherently form during the sputtering of MoS_2 and also be generated as a result of sliding-induced damage,[29,65] it is reasonable to attribute the increased friction under humid conditions to the formation of interfacial hydrogen bonds through the physisorption of H_2O at these defect sites. This is also supported by a small activation energy of 0.165 eV that correlates well with the physisorption energy of H_2O on MoS_2 and a higher energy barrier for sliding MoS_2 layers with adsorbed H_2O than for pristine layers. Hence, the friction reduction of MoS_2 with increased temperature under a humid environment in Figure 2 could be attributed to the thermal-activated reduction in the amount of interfacial hydrogen bonds via desorption of H_2O from MoS_2 surfaces, where higher temperature leads to a lower amount of H_2O adsorption and lesser interfacial H⋯S hydrogen bonds impeding layer sliding.

The DFT studies revealed H_2O adsorbed undissociatively at V_S, V_{S2}, V_{MoS}, V_{MoS3}, and V_{Mo} sites of MoS_2 with Ea values of −0.56 ∼ −0.17 eV, agreeing with Ea values of −0.15 eV for H_2O physisorption on the surface of MoS_2 and of −1.34 to −0.43 eV for H_2O dissociative adsorption at edge sites of MoS_2 in reference 33. Besides physisorption of H_2O, it is noted from references 29,30 that H_2O dissociative adsorption at the most reactive V_{MoS2} vacancy would occur with small activation

energy required, which would lead to the formation of Mo−O bonds that may serve as an initial step for oxidation of MoS_2 to form MoO_3. Previous experiments and molecular dynamics simulations by Curry et al.[26] also confirmed that oxidation of MoS_2 occurred primarily at the top layer of MoS_2 in highly reactive environments of atomic oxygen and molecule oxygen at 250 °C. Considering that the continuous oxidation process to form MoO_3 requires removal of S and diffusion of O, which could be a rate-limited process, oxidation of MoS_2 in the current study under a humidity of <40% and a low load of 0.3 N was expected to proceed at a slow rate as a result of less structural destruction by a small friction force with fewer H_2O molecules supplied than the ones in high-humidity environments. The physisorption of H_2O onto MoS_2 at low humidity levels without significant oxidation is in alignment with the Raman and TEM observations. Thus, the friction increase in humid environments observed in the study is mainly attributed to the effect of physisorption of H_2O. The desorption analysis and Arrhenius analysis showed that the nature of this H_2O adsorption process is reversible as heating to elevated temperatures to thermally desorb H_2O from surfaces of MoS_2. The common activation energy of 0.165 eV from Arrhenius analyses indicated that the operating friction mechanism of MoS_2 stays unchanged in both environments with 20% RH and 40% RH. Comparing the activation energy of 0.165 eV with the computed Ea values from DFT, it can be noted that they fall within the same range despite different approaches being used. Thus, it can be assured that the adsorption of H_2O is responsible for the increased friction of MoS_2. Previously, the molecular dynamics simulations by Onodera et al.[66] showed that the low friction between MoS_2 layers largely resulted from Coulombic repulsion between S atoms and the friction depends highly on interlayer contacts.[67] This study revealed that the formation of new interfacial bonds by the H_2O adsorption at defects would also be able to dominate friction of MoS_2 by increasing the E_B value and impeding layer sliding. However, it should also be noted that the interlayer sliding simulations are performed to show that H_2O adsorption would be able to alter the layer sliding performances, and the sliding energy barrier is subjected to change if the interface registry differs, such as layer stacking and rotation of the interfacial layer. Meanwhile, this work has shown the formation of interfacial H⋯S hydrogen bonds in vacancy-defected MoS_2 with low H_2O coverage through DFT computations. Future studies, both experimental and simulation-based, are needed to explore the detailed mechanisms of hydrogen bond formation at other defects, such as edges and antisites, particularly under higher H_2O coverage.

4. CONCLUSIONS

In this study, the increased friction of MoS_2 under humid conditions, a phenomenon conventionally attributed to the formation of MoO_3 through tribo-chemical processes, was explored. By conducting a combination of sliding friction experiments at different temperatures and employing DFT computations, it has been demonstrated in this study that the increase in the COF of MoS_2 in a humid environment can be primarily attributed to the adsorption of H_2O molecules, resulting in the formation of physical bonds between MoS_2 layers. This process exhibits reversibility, with friction reduction observed upon H_2O desorption. DFT computations revealed the stability of physisorbed H_2O at defect sites, forming interfacial hydrogen bonds with MoS_2. Sliding friction

tests conducted in dry air at 25 and 120 °C demonstrated low coefficients of friction (COF) of 0.02, suggesting that oxidation and film softening at these temperatures do not significantly affect friction.

Raman and TEM analyses have confirmed that MoS_2 layers near the contact surface became parallel to the sliding interface during the sliding process. However, this parallel layer orientation alone did not fully account for the low friction observed in humid conditions. In sliding tests conducted at 20 and 40% RH and elevated temperatures, the COF consistently showed a decreasing trend. Notably, the activation energy remained similar at both RH levels, with a constant value of 0.165 eV. This alignment with the computed H_2O adsorption energy range of −0.56 to −0.17 eV suggests that H_2O desorption from the MoS_2 surface is more likely to occur at sites characterized by relatively high adsorption energies. Thus, during the sliding process in a humid environment, where a new interface forms at the leading edge of the sliding direction, DFT studies have revealed that the disruption of the interfacial hydrogen bond formed between H_2O and MoS_2 requires a significantly greater additional energy input. This additional energy dissipation leads to an increase in friction.

Overall, this study establishes a theoretical and experimental foundation for designing interfaces that can enhance or inhibit hydrogen bonds in MoS_2 films, enabling their functionality for various applications. Understanding these principles aids in the development of innovative materials and surfaces with tailored properties to meet specific needs.

◼ ASSOCIATED CONTENT

ⓈⒾ Supporting Information

The Supporting Information is available free of charge at https://pubs.acs.org/doi/10.1021/acsami.3c18533.

> Raman spectra of the as-deposited MoS_2 film and MoS_2 powder before and after ball milling, atomic structures with H_2O placed at the V_{MoS3} defect site of MoS_2 with different initial H_2O orientations; TG-DTG of MoS_2 powder before and after ball milling, friction curves of MoS_2 tested at 25−100 °C under 20% RH, SEM-EDS mapping of the wear track tested at 25 °C under 40% RH, total and projected electronic density of state plots of H_2O adsorption at defect sites of MoS_2, and net charge distribution of oxygen and hydrogen from H_2O adsorbed on MoS_2 (PDF)

◼ AUTHOR INFORMATION

Corresponding Authors

Bin Zhang − *State Key Laboratory of Solid Lubrication, Lanzhou Institute of Chemical Physics, Chinese Academy of Sciences, Lanzhou 730000, China; Center of Materials Science and Optoelectronics Engineering, University of Chinese Academy of Sciences, Beijing 100049, China;* ⓞ orcid.org/0000-0002-9038-7514; Email: bzhang@licp.cas.cn

Junyan Zhang − *State Key Laboratory of Solid Lubrication, Lanzhou Institute of Chemical Physics, Chinese Academy of Sciences, Lanzhou 730000, China; Center of Materials Science and Optoelectronics Engineering, University of Chinese Academy of Sciences, Beijing 100049, China;* Email: zhangjunyan@licp.cas.cn

Ahmet T. Alpas − *Tribology of Materials Research Centre, Department of Mechanical, Automotive & Materials*

Engineering, University of Windsor, Windsor, Ontario N9B 3P4, Canada; Email: aalpas@uwindsor.ca

Authors

Zaixiu Yang − *State Key Laboratory of Solid Lubrication, Lanzhou Institute of Chemical Physics, Chinese Academy of Sciences, Lanzhou 730000, China;* ⓞ orcid.org/0000-0001-7760-6295

Xingkai Zhang − *State Key Laboratory of Solid Lubrication, Lanzhou Institute of Chemical Physics, Chinese Academy of Sciences, Lanzhou 730000, China*

Kaixiong Gao − *State Key Laboratory of Solid Lubrication, Lanzhou Institute of Chemical Physics, Chinese Academy of Sciences, Lanzhou 730000, China*

Fatih G. Sen − *Novelis Global Research and Technology Center, Kennesaw, Georgia 30144, United States*

Sukanta Bhowmick − *Tribology of Materials Research Centre, Department of Mechanical, Automotive & Materials Engineering, University of Windsor, Windsor, Ontario N9B 3P4, Canada*

Complete contact information is available at:
https://pubs.acs.org/10.1021/acsami.3c18533

Author Contributions

The article was written through contributions of all authors. All authors have given approval to the final version of the article.

Notes

The authors declare no competing financial interest.

◼ ACKNOWLEDGMENTS

◼ REFERENCES

(1) Liu, B. L.; Chen, L.; Liu, G.; Abbas, A. N.; Fathi, M.; Zhou, C. W. High-performance chemical sensing using Schottky-contacted chemical vapor deposition grown monolayer MoS_2 transistors. *ACS Nano* **2014**, *8* (5), 5304−5314.

(2) Wang, B.; Li, H.; Tan, H.; Gu, Y.; Chen, L.; Ji, L.; Sun, Z.; Sun, Q.; Ding, S.; Zhang, D. W.; Zhu, H. Gate-modulated high-response field-effect transistor-type gas sensor based on the MoS_2/metal-organic framework heterostructure. *ACS Appl. Mater. Interfaces* **2022**, *14* (37), 42356−42364.

(3) Scharf, T. W.; Prasad, S. Solid lubricants: A review. *J. Mater. Sci.* **2013**, *48* (2), 511−531.

(4) Ma, T.; Liu, Y.; Li, Q.; Luo, J. Toward Micro- and Nanoscale Robust Superlubricity by 2D Materials. In *Superlubricity*; Elsevier, 2021; pp 131−144.

(5) Roberts, E. Thin solid lubricant films in space. *Tribol. Int.* **1990**, *23* (2), 95−104.

(6) Chianelli, R. R.; Prestridge, E.; Pecoraro, T.; DeNeufville, J. Molybdenum disulfide in the poorly crystalline "Rag" structure. *Science* **1979**, *203* (4385), 1105−1107.

(7) Hoffman, E. E.; Marks, L. D. Soft interface fracture transfer in nanoscale MoS$_2$. *Tribol. Lett.* **2016**, *64* (1), 16.

(8) Cahangirov, S.; Ataca, C.; Topsakal, M.; Sahin, H.; Ciraci, S. Frictional figures of merit for single layered nanostructures. *Phys. Rev. Lett.* **2012**, *108* (12), No. 126103.

(9) Hiraoka, N. Wear life mechanism of journal bearings with bonded MoS$_2$ film lubricants in air and vacuum. *Wear* **2001**, *249* (10−11), 1014−1020.

(10) Cannon, P.; Norton, F. J. Reaction between molybdenum disulphide and water. *Nature* **1964**, *203* (4946), 750−751.

(11) Ross, S.; Sussman, A. Surface oxidation of molybdenum disulfide. *J. Phys. Chem. A* **1955**, *59* (9), 889−892.

(12) Lince, J. R.; Loewenthal, S. H.; Clark, C. S. Tribological and chemical effects of long term humid air exposure on sputter-deposited nanocomposite MoS$_2$ coatings. *Wear* **2019**, *432−433*, No. 202935.

(13) Stewart, T. B.; Fleischauer, P. D. Chemistry of sputtered molybdenum-disulfide films. *Inorg. Chem.* **1982**, *21* (6), 2426−2431.

(14) Liang, T.; Sawyer, W. G.; Perry, S. S.; Sinnott, S. B.; Phillpot, S. R. First-principles determination of static potential energy surfaces for atomic friction in MoS$_2$ and MoO$_3$. *Phys. Rev. B* **2008**, *77* (10), No. 104105.

(15) Berman, D.; Erdemir, A.; Sumant, A. V. Approaches for Achieving Superlubricity in Two-Dimensional Materials. *ACS Nano* **2018**, *12* (3), 2122−2137.

(16) Muratore, C.; Bultman, J. E.; Aouadi, S. M.; Voevodin, A. A. In situ Raman spectroscopy for examination of high temperature tribological processes. *Wear* **2011**, *270* (3−4), 140−145.

(17) Fleischauer, P. D.; Lince, J. R. A comparison of oxidation and oxygen substitution in MoS$_2$ solid film lubricants. *Tribol. Int.* **1999**, *32* (11), 627−636.

(18) Haltner, A. J.; Oliver, C. Effect of water vapor on friction of molybdenum disulfide. *Ind. Eng. Chem. Fund.* **1966**, *5* (3), 348−355.

(19) Zhao, X.; Perry, S. S. The role of water in modifying friction within MoS$_2$ sliding interfaces. *ACS Appl. Mater. Interfaces* **2010**, *2* (5), 1444−1448.

(20) Serpini, E.; Rota, A.; Valeri, S.; Ukraintsev, E.; Nicolini, P.; et al. Nanoscale frictional properties of ordered and disordered MoS$_2$. *Tribol. Int.* **2019**, *136*, 67−74.

(21) Kubart, T.; Polcar, T.; Kopecký, L.; Novak, R.; Novakova, D. Temperature dependence of tribological properties of MoS$_2$ and MoSe$_2$ coatings. *Surf. Coat. Technol.* **2005**, *193* (1−3), 230−233.

(22) Khare, H. S.; Burris, D. The effects of environmental water and oxygen on the temperature-dependent friction of sputtered molybdenum disulfide. *Tribol. Lett.* **2013**, *52* (3), 485−493.

(23) Addou, R.; Colombo, L.; Wallace, R. M. Surface Defects on Natural MoS$_2$. *ACS Appl. Mater. Interfaces* **2015**, *7* (22), 11921−11929.

(24) Hong, J.; Hu, Z.; Probert, M.; Li, K.; Lv, D.; Yang, X.; Gu, L.; Mao, N.; Feng, Q.; Xie, L.; et al. Exploring atomic defects in molybdenum disulphide monolayers. *Nat. Commun.* **2015**, *6*, No. 6293.

(25) Zhou, W.; Zou, X. L.; Najmaei, S.; Liu, Z.; Shi, Y. M.; Kong, J.; Lou, J.; Ajayan, P. M.; Yakobson, B. I.; Idrobo, J. C. Intrinsic Structural Defects in Monolayer Molybdenum Disulfide. *Nano Lett.* **2013**, *13* (6), 2615−2622.

(26) Curry, J. F.; Wilson, M. A.; Luftman, H. S.; Strandwitz, N. C.; Argibay, N.; Chandross, M.; Sidebottom, M. A.; Krick, B. A. Impact of microstructure on MoS$_2$ oxidation and friction. *ACS Appl. Mater. Interfaces* **2017**, *9* (33), 28019−28026.

(27) Farigliano, L. M.; Paredes-Olivera, P. A.; Patrito, E. M. Oxidative etching of S-vacancy defective MoS$_2$ monolayer upon reaction with O$_2$. *Phys. Chem. Chem. Phys.* **2021**, *23* (17), 10225−10235.

(28) Ghuman, K. K.; Yadav, S.; Singh, C. V. Adsorption and dissociation of H$_2$O on monolayered MoS$_2$ edges: Energetics and mechanism from ab Initio simulations. *J. Phys. Chem. C* **2015**, *119* (12), 6518−6529.

(29) Yang, Z.; Bhowmick, S.; Sen, F. G.; Alpas, A. T. Microscopic and atomistic mechanisms of sliding friction of MoS$_2$: Effects of undissociated and dissociated H$_2$O. *Appl. Surf. Sci.* **2021**, *563*, No. 150270.

(30) Ataca, C.; Ciraci, S. Dissociation of H$_2$O at the vacancies of single-layer MoS$_2$. *Phys. Rev. B* **2012**, *85* (19), No. 195410.

(31) Levita, G.; Righi, M. C. Effects of water intercalation and tribochemistry on MoS$_2$ lubricity: an ab initio molecular dynamics investigation. *ChemPhysChem* **2017**, *18* (11), 1475−1480.

(32) Stella, M.; Lorenz, C. D.; Righi, M. C. Effects of intercalated water on the lubricity of sliding layers under load: a theoretical investigation on MoS$_2$. *2D Mater.* **2021**, *8* (3), No. 035052.

(33) Levita, G.; Restuccia, P.; Righi, M. C. Graphene and MoS$_2$ interacting with water: A comparison by ab initio calculations. *Carbon* **2016**, *107*, 878−884.

(34) Mignuzzi, S.; Pollard, A. J.; Bonini, N.; Brennan, B.; Gilmore, I. S.; Pimenta, M. A.; Richards, D.; Roy, D. Effect of disorder on Raman scattering of single-layer MoS$_2$. *Phys. Rev. B* **2015**, *91* (19), No. 195411.

(35) Parkin, W. M.; Balan, A.; Liang, L.; Das, P. M.; Lamparski, M.; Naylor, C. H.; Rodríguez-Manzo, J. A.; Johnson, A. T. C.; Meunier, V.; Drndić, M. Raman Shifts in Electron-Irradiated Monolayer MoS$_2$. *ACS Nano* **2016**, *10* (4), 4134−4142.

(36) Lee, J.-Y.; Kim, J. H.; Jung, Y.; Shin, J. C.; Lee, Y.; Kim, K.; Kim, N.; van der Zande, A. M.; Son, J.; Lee, G.-H. Evolution of defect formation during atomically precise desulfurization of monolayer MoS$_2$. *Commun. Mater.* **2021**, *2* (1), 80.

(37) Kresse, G.; Furthmüller, J. Efficiency of ab-initio total energy calculations for metals and semiconductors using a plane-wave basis set. *Comput. Mater. Sci.* **1996**, *6* (1), 15−50.

(38) Perdew, J. P.; Chevary, J. A.; Vosko, S. H.; Jackson, K. A.; Pederson, M. R.; Singh, D. J.; Fiolhais, C. Atoms, molecules, solids, and surfaces: Applications of the generalized gradient approximation for exchange and correlation. *Phys. Rev. B* **1992**, *46* (11), 6671.

(39) Perdew, J. P.; Burke, K.; Ernzerhof, M. Generalized gradient approximation made simple. *Phys. Rev. Lett.* **1996**, *77* (18), 3865.

(40) Lee, K.; Murray, É. D.; Kong, L.; Lundqvist, B. I.; Langreth, D. C. Higher-accuracy van der Waals density functional. *Phys. Rev. B* **2010**, *82* (8), No. 081101.

(41) Dion, M.; Rydberg, H.; Schroder, E.; Langreth, D. C.; Lundqvist, B. I. Van der Waals density functional for general geometries. *Phys. Rev. Lett.* **2004**, *92* (24), No. 246401.

(42) Klimeš, J.; Bowler, D. R.; Michaelides, A. Chemical accuracy for the van der Waals density functional. *J. Phys.: Condens. Matter* **2010**, *22* (2), No. 022201.

(43) Hamada, I. van der Waals density functional made accurate. *Phys. Rev. B* **2014**, *89* (12), No. 121103.

(44) Berland, K.; Cooper, V. R.; Lee, K.; Schröder, E.; Thonhauser, T.; Hyldgaard, P.; Lundqvist, B. I. van der Waals forces in density functional theory: a review of the vdW-DF method. *Rep. Prog. Phys.* **2015**, *78* (6), No. 066501.

(45) Tan, C. L.; Luo, Z. M.; Chaturvedi, A.; Cai, Y. Q.; Du, Y. H.; Gong, Y.; Huang, Y.; Lai, Z. C.; Zhang, X.; Zheng, L. R.; Qi, X. Y.; Goh, M. H.; Wang, J.; Han, S. K.; Wu, X. J.; Gu, L.; Kloc, C.; Zhang, H. Preparation of High-Percentage 1T-Phase Transition Metal Dichalcogenide Nanodots for Electrochemical Hydrogen Evolution. *Adv. Mater.* **2018**, *30* (9), No. 1705509.

(46) Pizzochero, M.; Yazyev, O. V. Point defects in the 1T' and 2H phases of single-layer MoS$_2$: A comparative first-principles study. *Phys. Rev. B* **2017**, *96* (24), No. 245402.

(47) Xia, M.; Li, B.; Yin, K. B.; Yin, K.; Capellini, G.; Capellini, G.; Niu, G.; Niu, G.; Gong, Y. J.; Gong, Y.; Zhou, W.; Zhou, W.; Ajayan, P. M.; Ajayan, P. M.; Xie, Y. H. Spectroscopic Signatures of AA' and AB Stacking of Chemical Vapor Deposited Bilayer MoS$_2$. *ACS Nano* **2015**, *9* (12), 12246−12254.

(48) Cortés, N.; Rosales, L.; Orellana, P. A.; Ayuela, A.; Gonzalez, J. W. Stacking change in MoS_2 bilayers induced by interstitial Mo impurities. *Sci. Rep.* **2018**, *8*, No. 2143.

(49) Pondick, J. V.; Woods, J. M.; Xing, J.; Zhou, Y.; Cha, J. J., Stepwise Sulfurization from MoO_3 to MoS_2 via Chemical Vapor Deposition. *ACS Appl. Nano Mater.* **2018**, *1* (10), 5655−5661.

(50) Vogl, L. M.; Schweizer, P.; Wu, M. J.; Spiecker, E. Transforming layered MoS_2 into functional MoO_2 nanowires. *Nanoscale* **2019**, *11* (24), 11687−11695.

(51) Yang, Q.; Sun, P. Z.; Fumagalli, L.; Stebunov, Y. V.; Haigh, S. J.; Zhou, Z. W.; Grigorieva, I. V.; Wang, F. C.; Geim, A. K. Capillary condensation under atomic-scale confinement. *Nature* **2020**, *588* (7837), 250−253.

(52) Wang, E. Z.; Xiong, Z. X.; Chen, Z. K.; Xin, Z. Q.; Ma, H. C.; Ren, H. T.; Wang, B. L.; Guo, J.; Sun, Y. F.; Wang, X. W.; Li, C. Y.; Li, X. Y.; Liu, K. Water nanolayer facilitated solitary-wave-like blisters in MoS_2 thin films. *Nat. Commun.* **2023**, *14* (1), No. 4324.

(53) Jinesh, K. B.; Frenken, J. W. M. Capillary condensation in atomic scale friction: How water acts like a glue. *Phys. Rev. Lett.* **2006**, *96* (16), No. 166103.

(54) Dickrell, P. L.; Pal, S. K.; Bourne, G. R.; Muratore, C.; Voevodin, A. A.; Ajayan, P. M.; Schadler, L. S.; Sawyer, W. G. Tunable friction behavior of oriented carbon nanotube films. *Tribol. Lett.* **2006**, *24* (1), 85−90.

(55) Zhao, X. Y.; Phillpot, S. R.; Sawyer, W. G.; Sinnott, S. B.; Perry, S. S. Transition from Thermal to Athermal Friction under Cryogenic Conditions. *Phys. Rev. Lett.* **2009**, *102* (18), No. 186102.

(56) Li, Q.; Zheng, S.; Pu, J.; Wang, W.; Li, L.; Wang, L. Revealing the failure mechanism and designing protection approach for MoS_2 in humid environment by first-principles investigation. *Appl. Surf. Sci.* **2019**, *487*, 1121−1130.

(57) González, C.; Biel, B.; Dappe, Y. J. Adsorption of small inorganic molecules on a defective MoS_2 monolayer. *Phys. Chem. Chem. Phys.* **2017**, *19* (14), 9485−9499.

(58) Jia, Q.; Yang, Z.; Zhang, B.; Gao, K.; Sun, L.; Zhang, J. Macro superlubricity of two-dimensional disulphide/amorphous carbon heterogeneous via tribochemistry. *Mater. Today Nano* **2023**, *21*, No. 100286.

(59) Hardcastle, F. D.; Wachs, I. E. Determination of molybdenum−oxygen bond distances and bond orders by Raman spectroscopy. *J. Raman Spectrosc.* **1990**, *21* (10), 683−691.

(60) Momma, K.; Izumi, F. VESTA3 for three-dimensional visualization of crystal, volumetric and morphology data. *J. Appl. Crystallogr.* **2011**, *44*, 1272−1276.

(61) Tang, W.; Sanville, E.; Henkelman, G. A grid-based Bader analysis algorithm without lattice bias. *J. Phys.: Condens. Matter* **2009**, *21* (8), No. 084204.

(62) Sanville, E.; Kenny, S. D.; Smith, R.; Henkelman, G. Improved grid-based algorithm for Bader charge allocation. *J. Comput. Chem.* **2007**, *28* (5), 899−908.

(63) Henkelman, G.; Arnaldsson, A.; Jonsson, H. A fast and robust algorithm for Bader decomposition of charge density. *Comput. Mater. Sci.* **2006**, *36* (3), 354−360.

(64) Levita, G.; Cavaleiro, A.; Molinari, E.; Polcar, T.; Righi, M. C. Sliding properties of MoS_2 layers: Load and interlayer orientation effects. *J. Phys. Chem. C* **2014**, *118* (25), 13809−13816.

(65) Bhowmick, S.; Banerji, A.; Alpas, A. Friction reduction mechanisms in multilayer graphene sliding against hydrogenated diamond-like carbon. *Carbon* **2016**, *109*, 795−804.

(66) Onodera, T.; Morita, Y.; Suzuki, A.; Koyama, M.; Tsuboi, H.; Hatakeyama, N.; Endou, A.; Takaba, H.; Kubo, M.; Dassenoy, F.; Minfray, C.; Joly-Pottuz, L.; Martin, J. M.; Miyamoto, A. A Computational Chemistry Study on Friction of h-MoS_2. Part I. Mechanism of Single Sheet Lubrication. *J. Phys. Chem. B* **2009**, *113* (52), 16526−16536.

(67) Onodera, T.; Morita, Y.; Nagumo, R.; Miura, R.; Suzuki, A.; Tsuboi, H.; Hatakeyama, N.; Endou, A.; Takaba, H.; Dassenoy, F.; Minfray, C.; Joly-Pottuz, L.; Kubo, M.; Martin, J. M.; Miyamoto, A. A Computational Chemistry Study on Friction of h-MoS_2. Part II. Friction Anisotropy. *J. Phys. Chem. B* **2010**, *114* (48), 15832−15838.